A New Mover Separated Linear Magnetic-Field Modulated Motor for Long Stroke Applications

Wenxiang Zhao, *Senior member, IEEE,* Shiyuan Wang, Jinghua Ji, Liang Xu, and Zhijian Ling

[1]School of Electrical and Information Engineering, Jiangsu University, Zhenjiang 212013, China
[2]Jiangsu Key Laboratory of Drive and Intelligent Control for Electric Vehicle, Zhenjiang 212013, China

Linear magnetic-field modulated (LMFM) motor exhibits high thrust force by effectively employing the magnetic-field modulation effect. In this paper, a new mover separated linear magnetic-field modulated (MS-LMFM) motor is proposed, which successfully alleviates the space confliction between PMs and windings in the existing LMFM motor. The structure and the operation principle of the existing and proposed motor are described and the major design parameters are optimized for maximum thrust force. Moreover, electromagnetic performances of both motors are compared by finite element method. Theoretical and simulation analysis shows that the proposed motor can exhibit enhanced force performance than the existing one under fixed copper loss. Simultaneously, reduced iron and PM losses can also be obtained by proposed motor. Finally, a three dimensional (3D) modeling MS-LMFM motor is built for a global observation of motor structure and further verification of the two dimensional (2D) analysis.

Index Terms—**Finite element method, linear motor, magnetic-field modulation, separated mover.**

I. INTRODUCTION

COMPARED WITH traction systems which apply conventional rotary motors, linear induction motors possess the merits to eliminate the bulky rotary-to-linear mechanism [1]. Therefore, numerous energy transformation steps can be reduced. However, linear induction motors suffer from a serious problem of relatively low efficiency. Recently, the utilization of high energy rare-earth permanent magnets (PMs) has significantly improved the efficiency of motor, but it is still insufficient for some high thrust force applications. To solve this problem, magnetic-field modulation effect can be artfully employed in the linear magnetic-field modulated (LMFM) motor to effectively improve the thrust force [2], [3].

In the existing LMFM motor, the PMs and the armature windings are mounted on the short mover and the long stator consists of iron only [4]. Therefore, the existing motor incorporates the merits of high thrust force and low cost simultaneously, which is suitable for long stroke applications. Moreover, appropriate Halbach PM arrays are mounted on the mover surface of existing motor in order to reduce the PM fringing flux leakages. However, the space confliction between the magnetic and electrical loadings should be considered as the main shortcoming of existing motor. This is because its excitation sources, including the PMs and windings, are placed on its limited mover area. In order to alleviate the geometric space confliction between these two kinds of excitation sources, a new mover separated LMFM (MS-LMFM) motor will be proposed in this paper, which effectively separates the PMs and windings on the partitioned movers and its stator is also simple iron core only with salient poles. Therefore, compared with the existing motor, the proposed motor could allow higher electric load and will further improve the thrust force without extra cost, which is more suitable for long stroke applications. In fact, several investigations have been carried out on separation in the conventional rotary PM motors [5], [6], but there is no generally accepted theory concerning employing separation in

the LMFM motor. Considering the modulation effect and special motor structure of the LMFM motor, its mover separation deserves attention. The purpose of this paper is to investigate the separation effects on performances of LMFM motor and further highlight the improvements in the proposed motor. This paper is organized as follows. The topology and the operation principle of the existing LMFM and proposed MS-LMFM motor will be briefly described in Section II. Section III will be devoted to introduce the optimization process and investigate the performances of both motors by using finite element (FE) method. In addition, the theoretical analysis of enhanced force in the proposed motor is also given. Furthermore, a three dimensional (3D) modeling MS-LMFM motor will be investigated for global observation of novel motor structure and verification of the two dimensional (2D) FE analysis in Section IV. Finally, conclusions will be summarized in Section V.

II. TOPOLOGY AND OPERATION PRINCIPLE

In Fig. 1(a), the cross section of the existing three phase 20/18 stator/mover-pole LMFM motor is presented. Furthermore, the existing motor will be expanded to MS topology in this section. The proposed MS-LMFM motor is shown in Fig. 1(b). It is noted that the proposed motor consists of one stator and two movers, and the concentrated windings and PMs are separated from the single mover of existing
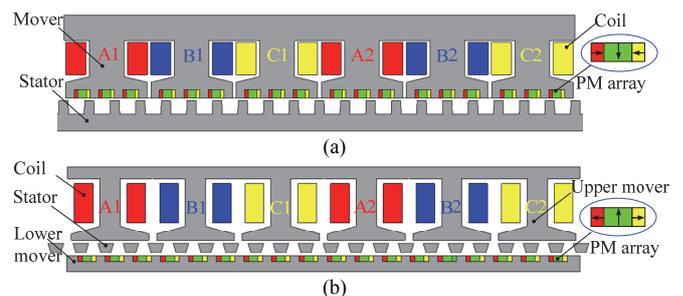

Fig. 1. Cross section. (a) Existing motor. (b) Proposed motor.

motor and placed on the upper mover and lower mover, respectively. Moreover, the long stator in the proposed motor consists of only iron pieces, which are sandwiched between the upper mover and the lower mover. It is illustrated that the two movers move in the same direction and at identical speed. Additionally, in the existing motor, the excitation sources of PMs and windings will contend for the limited mover area. Benefited from the artfully partition of mover, the proposed motor has the feature of larger slot area, which allows higher electric load and will further enhance the thrust force under the same motor volume. In the existing motor, the magnetic fields produced by windings and PMs have strong coupling because these two excitations are in narrow single mover area. When the current is very high, the winding magnetic motive force (MMF) will affect the PM normal working condition and may generate risk of PM irreversible demagnetization. However, there exists stator teeth and two air gaps between these two excitations in the proposed motor, the strong coupling is weakened and the winding MMF can operate with modulated flux in upper air gap, which has slight effect on PMs. Therefore, the PM irreversible demagnetization risk can be reduced [7]. It is demonstrated from Fig. 2, which reveals the detailed flux density distributions in PMs of both motors at rated loads and overloads to further observe the partial demagnetization. It is noted that the worst demagnetization occurs in the existing motor when it operates at fourfold overload, which is marked in red circle. Whereas, the partial demagnetization in the proposed motor is very slight, which can even be ignored. Hence, the PMs of the proposed motor are relatively safe when it operates at rated load and overload. Also, it is noticed that numerous Halbach PM arrays are mounted on the surface of mover in the existing motor and on that of lower mover in the proposed motor. In fact, a Halbach PM array has three segments, whose magnetization directions differ from each other and only has two regular magnetizing patterns [8], which are explicitly plotted by color and referred by arrows. Actually, the radially magnetized PMs are sandwiched between two tangentially magnetized PMs, which can mitigate PM fringing flux leakages and focus fluxes for higher flux density. In addition, the sandwiched stator teeth of the proposed motor will act as the modulation ferromagnetic pole pieces to effectively modulate the magnetic field, which has similar function with the stator teeth of the existing motor. The basic magnetic-field modulation principle can be expressed as：

$$p_w = \left| p_{PM} - n_s \right| \qquad (1)$$

where p_w, p_{PM} and n_s are the pole-pair number of windings, the pole-pair number of the PM magnetic field and the active number of the stator teeth, respectively. In both motors, the PM pole-pair number is 18 and when the PM excites independently, both motors exhibit significant 2 pole-pair distribution as shown in Fig. 3, which is identical with the winding pole-pair number. Moreover, the magnetic field excited by PMs will be modulated in upper air gap by 20 stator modulated teeth to produce significantly high amplitude 2 pole-pair harmonic to corporate with the winding MMF. The

modulated harmonic is marked in blue circle in Fig. 4(b), which presents the harmonic analysis of flux density and the flux density is shown in Fig. 4(a). Similarly, it is evident that when only windings are excited, the 18 pole-pair number modulated harmonic marked in red circle will be produced in lower air gap to operate with PMs. Therefore, both motors will yield a steady and high thrust force by synchronizing the winding magnetic motive force to the flux moving by magnetic-field modulation.

III. OPTIMIZATION AND PERFORMANCES ANALYSIS

Owing to the effective separation of mover, the structure of proposed motor has significant variation compared with the existing motor. Thus, several parameters deserve redesigning and optimizing. Also, the motor volume, PM consumption, slot/pole-combination and air gap length are fixed for a fair comparison and other parameters are optimized for maximum thrust force under current of 5 A. The relationship between the thrust force and the stator top tooth width ratio is investigated in Fig. 5, which is defined as the ratio of stator top tooth width to the stator pole pitch. The stator top tooth width ratio is closely associated with the variation of force and the thrust force will decrease gradually over the optimized value of 0.63 Moreover, the stator bottom tooth width ratio effects on the force of proposed motor should be optimized synchronously. It is found that when the stator bottom tooth width ratio,
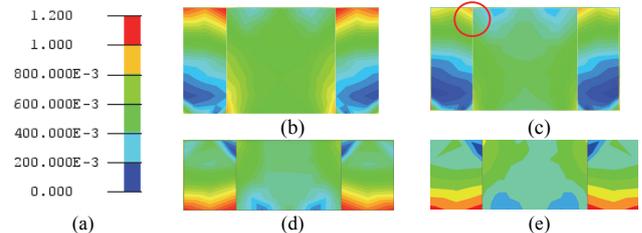

Fig. 2. Flux density distributions in PMs at the worst demagnetization of both motors. (a) Color scale. (b) Existing motor at rated load. (c) Existing motor at overload. (d) Proposed motor at rated load. (e) Proposed motor at overload.
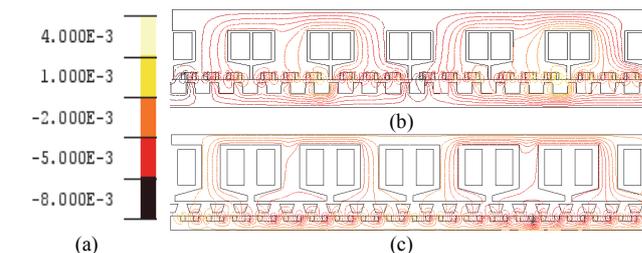

Fig. 3. Magnetic field distributions. (a) Color scale. (b) Existing. (c) Proposed.
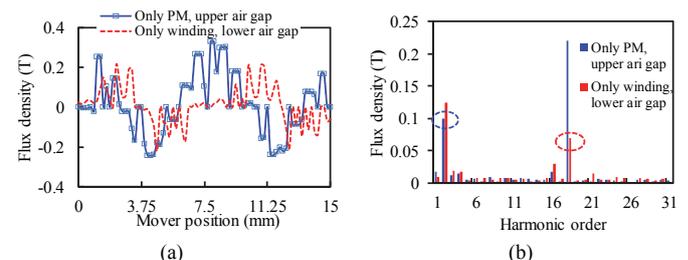

Fig. 4. Upper air gap flux density produced by only PMs and lower air gap flux density produced by only windings. (a) Waveform. (b) Harmonic analysis.
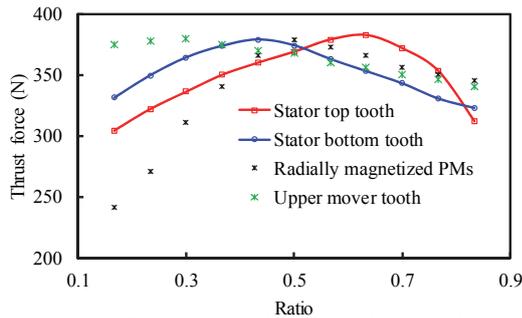
Fig. 5. Optimization of stator tooth width and radially magnetized PM width.

namely the ratio of stator bottom tooth width to the stator pole pitch, reaches 0.42, the maximum thrust force will be obtained. In fact, it is concluded that the final stator iron piece will be optimized to the shape of inverted trapezoid, which can facilitate the reduction of flux leakages. Furthermore, the PM parameters are the major lower mover parameters, which deserve much attention. It is evident that the force will increase dramatically and gradually reduce when the radially magnetized PM width ratio, namely the ratio of radially magnetized PM width to the PM array width, is over the optimized value of 0.5. Radially magnetized PM width should not be very small due to its major function of producing PM magnetic field. It is noted from Fig. 6 that the most optimized PM thickness is approximate 3.75 mm under the fixed PM consumption. The upper mover parameters are optimized by multiple variables. The upper mover width ratio is the ratio of upper mover tooth width to upper mover bottom tooth width and its optimized value is 0.3. Meanwhile, the optimization of upper mover slot opening width is equivalent to optimizing the bottom tooth width of upper mover. The maximum force can be obtained when it is 4.2 mm. The final optimized results and corresponding parameters of both motors are listed in Table I.

The three phase back-EMFs at speed of 1.5 m/s are shown in Fig. 7. It is observed that the proposed motor offers higher back-EMF. Furthermore, both motors exhibit sinusoidal and symmetric back-EMFs. The spectrum analysis of back-EMFs is investigated in Fig. 8. It is concluded that the fundamental harmonic is dominant, while other harmonics components are dramatically low. Also, the proposed motor produces negligible fifth- and seventh-order harmonics in the back-EMFs accounting for the limited curves distortion. Further observation reveals that the relatively low odd harmonics result in the sinusoidal back-EMFs. Fig. 9 shows the force performances of both motors. It is evident that the waveform slope of force with respect to current in the existing motor is relatively inferior to the proposed motor. Therefore, the proposed motor can exhibit better overload force capability. However, the waveforms slope of both motors tend to be gradual observably when the current is over the rated value of 5 A. It is remarkable that the force ripples remain relatively small when the current is close to the rated value. Simultaneously, compared with the existing motor, the proposed motor exhibits 9.3% higher thrust force with reduced force ripple at rated load. Moreover, the proposed motor can exhibit the same percent higher force density under identical

motor volume and its value is 163.6 kN/m3. Considering that the existing motor can already exhibit a very high force, the force improvement of proposed motor is more valuable. Moreover, to ensure the accuracy of FE analysis, a theoretical analysis of enhanced force in the proposed motor is also given.
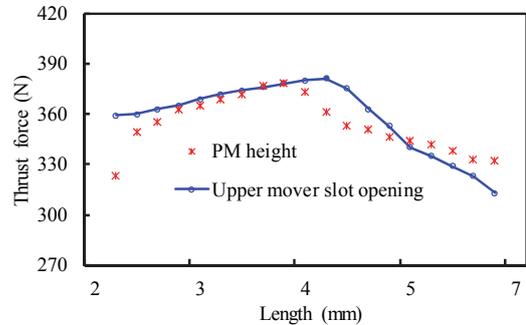

Fig. 6. Optimization of upper mover slot opening width and PM height.

TABLE I
DESIGN SPECIFICATIONS

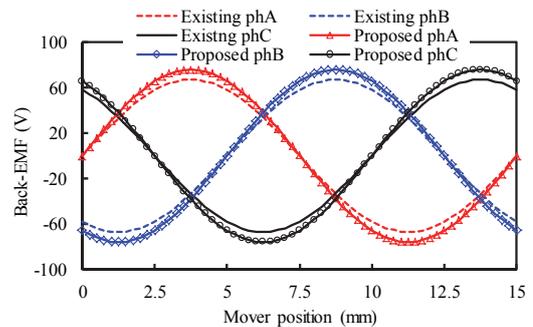| Items	Existing	Proposed
Motor volume (cm^3)	2340	
Upper mover tooth width (mm)	20	15
Upper mover slot opening width (mm)	2	4.2
Air gap length (mm)	2	Upper 2 Lower 2
Stator top tooth width (mm)	5.2	9.5
Stator bottom tooth width (mm)	---	6.3
PM consumption (cm^3)	243	
Radially magnetized PM width (mm)	5	6
PM array width (mm)	9	12
PM thickness (mm)	5	3.75
Stack length (mm)	300	
Copper mass (kg)	1.82	1.96
Total weight (kg)	17.2	17.3
Force of unit motor weight (N/kg)	20.3	21.9
Armature windings per coil, N	100	108

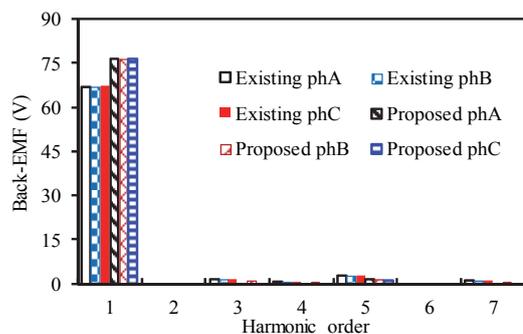Fig. 7. Back-EMFs of existing and proposed motor at speed of 1.5 m/s.
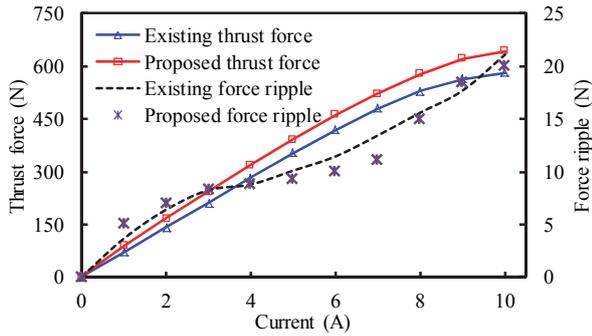

Fig. 8. Spectrum analysis of back-EMFs.

Fig. 9. Force and force ripple with respect to current.

In the LMFM motor, the relative air gap permeance can be expressed as:

$$\lambda = \lambda_0 + (-1)^m \lambda_1 \cos(N_w x) \quad (2)$$

where λ_0 and λ_1 are 0th and 1st order of λ, which can be calculated using conformal mapping method [9]:

$$\lambda_0 = \frac{\mu_0}{g + h_{PM}/\mu_r}(1 - 1.6\beta S_{op}/\tau_s) \quad (3)$$

$$\lambda_1 = \frac{2l_m}{\pi\tau_s}\int_0^{\frac{1.6\pi S_{op}}{l_m}}(1 - \beta - \beta\cos\frac{l_m}{1.6 S_{op}}x)$$

$$\cdot\cos\frac{l_m}{\tau_s}\mu_r x dx + \frac{2l_m}{\pi\tau_s}\int_{\frac{1.6\pi S_{op}}{l_m}}^{\frac{\pi\tau_s}{l_m}}\cos\frac{l_m}{\tau_s}\mu_r x dx \quad (4)$$

$$= \frac{4\beta}{\pi}\sin(1.6\pi S_{op}/\tau_s)\frac{0.5 + (S_{op}/\tau_s)^2}{0.78125 - 2(S_{op}/\tau_s)^2}$$

$$\beta = \frac{\mu_0}{g + h_{PM}/\mu_r}\left[0.5 - 0.5/(\sqrt{1 + (\frac{S_{op}}{2g + 2h_{PM}/\mu_r})^2}\right] \quad (5)$$

where m, x, g, τ_s, μ_0, μ_r and l_m are mover winding pitch, mover position, air gap length, stator pole pitch, the permeability of vacuum, relatively permeability and mover length, respectively. They are identical in both motors and the different parameters are S_{op} and h_{PM}, namely mover slot opening width and PM height. The working modulated magnetic field of LMFM motor is produced by PMs and modulated teeth, which can be expressed as:

$$B = B_n\lambda \quad (6)$$

where B_n is the no-load air gap flux densities of motor having no slots. Only considering its very dominant fundamental component, (6) can be rewritten as:

$$B = B_n\lambda(x) = B_{n1}\lambda\cos[p_{PM}(x - vt)]$$
$$= B_{PM}\lambda\cos[p_{PM}(x - vt)]$$
$$+ (-1)^m B_w\lambda\cos(p_w x + p_{PM}vt) \quad (7)$$
$$+ (-1)^m B_{n_s+PM}\lambda\cos[(p_{PM} + n_s)x - p_{PM}vt]$$

where B_{n1} is the fundamental component of B_n and its value approximates the PM remanence. Additionally, B_{PM}, B_w and B_{n_s+PM} are 18th, 2nd and 38th order modulated harmonics of magnetic field. They should meet:

$$\begin{cases} B_w = B_{n_s+PM} = B_{n1}\lambda_1/2 \\ B_{PM} = B_{n1}\lambda_0 \end{cases} \quad (8)$$

The flux linkage can be obtained by the integral of working

modulated magnetic field and the thrust force can be calculated according to the Faraday's law:

$$F = \frac{9.55 * 3I_m k_w l_m N_w l_{stk}}{2\sqrt{2}}(\frac{p_{PM}B_w}{p_w} + B_{PM} - \frac{p_{PM}B_{n_s+PM}}{p_{PM}+n_s}) \quad (9)$$

where I_m, k_w and l_{stk} are armature current, winding factor and the stack length. They are identical in both motors. When the mover position is fixed, the moving time t will be obtained under the same move speed of v. Therefore, the working modulated magnetic field can be calculated by (7) and (8) and it is associated with relative air gap permeance. It is noted from (3)-(5) that the relative air gap permeance is related to motor parameters and only slot opening width and PM height are different. Besides, the ratio of them between existing and proposed motor are 0.48 and 1.33. N_w is winding turns and it can be derived from (11) and (12). Considering these two parameters and the different winding turns, the force is improved about 9.31% by calculation from (9), which has a good agreement with FE analysis.

Except for the aforementioned performances of back-EMF and thrust force, loss is also important on-load characteristic of both motors and it is the essential index of performance evaluation. Therefore, the loss details of both motors are compared and analyzed.

To calculate the copper loss of the existing and proposed motor, the total length of windings should be determined at first. A simplified winding model, in which end-turns winding are assumed to be semicircular, is used to calculate the total winding length. The copper loss P_{Cu} of both motors can be expressed as follows:

$$P_{Cu} = \frac{I_m^2(l_{end} + l_{stk})N_w N_s\rho_{cu}}{A_{cond}} \quad (10)$$

where l_{end} is the end-winding length, N_s is the slot number, ρ_{cu} is the electrical resistivity of copper and A_{cond} is the area of per conductor.

In fact, in this paper, the copper loss herein of both motors is calculated as 41.2 W and will be fixed for a fair comparison, therefore:

$$A_{cond2} = \frac{A_{cond1}N_{w2}(l_{end2} + l_{stk})}{N_{w1}(l_{end1} + l_{stk})} \quad (11)$$

The separation of PMs and windings from the limited single mover area, is the novelty of proposed MS-LMFM motor, which effectively enlarges the slot area and adjusts the end-winding length, therefore:

$$N_{w2} = \frac{N_{w1}S_2 A_{cond1}}{S_1 A_{cond2}} \quad (12)$$

where A_{cond1}, N_{w1}, l_{end1} and S_1 are the per conductor area, winding turns, end-winding length and slot area of existing motor. Similarly, A_{cond2}, N_{w2}, l_{end2} and S_2 are that of proposed motor, respectively. Besides, the ratios of reduced end-winding length and enlarged slot area between existing and proposed motor are 0.58 and 1.36, respectively. Therefore, the winding turns of proposed motor can be artfully increased with fixed copper loss by adjusting per conductor area.

The PM loss and iron loss with respect to speed are evaluated by FE method, which is investigated in Fig. 10. It is

observed that both motors generate insignificant PM loss at low speed. However, when the speed is over the rated value of 1.5 m/s, the PM loss will ascend rapidly and it is significant in the existing motor that the PM loss will increase nearly four times, whereas the speed is only twice higher. It is explicitly shown in the partially enlarged figure of the area marked in rectangle. Furthermore, it is evident that the iron losses of both motors will deteriorate significantly when the speed is over 1.5 m/s [10]. However, the proposed motor generates comprehensively less PM and iron losses with respect to speed, which is especially obvious over the rated speed. It implies that the proposed motor can produce greatly improved force performances with superior loss performances. Simultaneously, this improvement tends to be more notable as speed increases. Therefore, the proposed motor can greatly reinforce the comprehensive performances by artfully mover separation and is more suitable for long stroke applications.

IV. VERIFICATION

In this section, a 3D modeling MS-LMFM motor is built in Fig. 11 to give a global observation of the novel structure of proposed motor. Also, the particular stator pole pieces can only be explicitly observed from the 3D model. In addition, the 3D modeling MS-LMFM motor has been investigated for further verification of the aforementioned 2D FE analysis. The thrust force and loss details at rated load of the existing and proposed motor, obtained by 2D and 3D FE analysis, are compared in Fig. 12. It deserves attention that the copper loss

is calculated by (2) and can be auxiliary simulated by FE method. It is observed that there is a good agreement between the 2D and 3D FE results and the proposed motor can greatly enhance the thrust force with reduced losses, which validates the former analysis and further highlights the superiority of mover separation.

V. CONCLUSION

In this paper, a novel MS-LMFM motor has been proposed and several varied geometric parameters have been optimized for maximum thrust force. Furthermore, a comparison between the proposed and existing motor has been carried out under fixed copper loss by FE method. Compared with the existing motor, it is confirmed that the irreversible demagnetization risk of the proposed motor is reduced. Also, the proposed motor can exhibit both greatly enhanced force performances and relatively small losses without extra cost, which is more suitable for high thrust force and long stroke applications. Finally, a 3D modeling MS-LMFM motor has been built and simulated, verifying the effectiveness of 2D FE analysis.
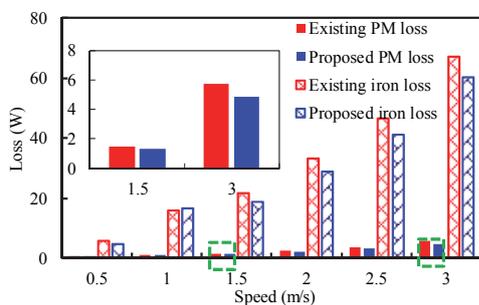
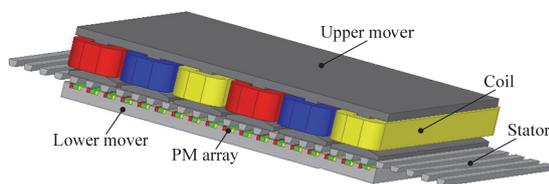Fig. 10. Loss details with respect to speed.

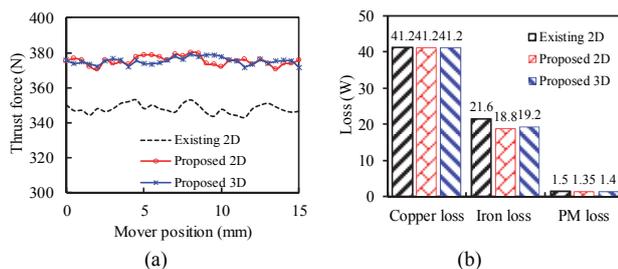Fig. 11. Three dimensional model of proposed motor.

Fig. 12. Comparison of 2D and 3D analysis. (a) Thrust force. (b) Loss details.

REFERENCES

[1] D. Li, W Li, J. Fang, X. Zhang, and J. Cao, "Performance evaluation of a low-speed single-side HTS linear induction motor used for subway system," *IEEE Trans. Magn.*, vol. 50, no. 5, Nov. 2014, Art. ID. 8201109.
[2] M. Cheng, P. Han, and W. Hua, "A general airgap field modulation theory for electrical machines," *IEEE Trans. Ind. Electron.*, DOI: 10.1109/TIE.2017.2682792, 2017.
[3] J. Bai, P. Zheng, L. Cheng, S. Zhang, J. Liu, and Z. Liu, "A new magnetic-field-modulated brushless double-rotor machine," *IEEE Trans. Magn.*, vol. 51, no. 11, Jun. 2015, Art. ID. 8112104.
[4] W. Zhao, J. Zheng, J. Wang, and et al, "Design and analysis of a linear permanent magnet vernier machine with improved force density," *IEEE Trans. Ind. Electron.*, vol. 63, no. 4, pp. 2072-2082, Apr. 2016.
[5] Z. Q. Zhu, Z. Wu, D. J. Evans, and W. Chu, "Novel electrical machines having separate PM excitation stator," *IEEE Trans. Magn.*, vol. 51, no. 4, Apr. 2015. Art. ID. 8104109.
[6] H. Hua, Z. Q. Zhu, and H. Zhan, "Novel consequent-pole hybrid excited machine with separated excitation stator," *IEEE Trans. Ind. Electron.*, vol. 63, no. 8, pp. 4718-4728, Apr. 2016.
[7] K. Guo, S. Fang, Y. Zhang, H. Yang, H. Lin, S. L. Ho, and N. Feng, "Irreversible demagnetization analysis of permanent magnet materials in a novel flux reversal linear-rotary permanent magnet actuator," *IEEE Trans. Magn.*, vol. 52, no. 7, Feb. 2016. Art. ID. 8202904.
[8] J. Chen, B. Zhang, and H. Ding, "Analysis of curve-edged halbach arrays in linear permanent-magnet actuators using the open boundary differential quadrature finite-element method," *IEEE Trans. Magn.*, vol. 52, no. 4, Oct. 2016. Art. ID. 7209411.
[9] Z. Q. Zhu, and D. Howe, "Instantaneous magnetic-field distribution in brushless permanent-magnet DC motors—Part III. Effect of stator slotting," *IEEE Trans. Magn.*, vol. 29, no. 1, pp. 143-151, Jan. 1993.
[10] S. Hwang, M. Lim, and J. Hong, "Hysteresis torque estimation method based on iron-loss analysis for permanent magnet synchronous motor," *IEEE Trans. Magn.*, vol. 52, no. 7, Feb. 2016. Art. ID. 8204904.